Applied Catalysis B: Environmental 328 (2023) 122448

Contents lists available at ScienceDirect

Applied Catalysis B: Environmental

journal homepage: www.elsevier.com/locate/apcatb

The interplay between dopant and a surface structure of the photocatalyst – The case study of Nb-doped faceted TiO_2

Szymon Dudziak [a,*], Ewa Kowalska [b,c], Kunlei Wang [b], Jakub Karczewski [d], Mirosław Sawczak [e], Bunsho Ohtani [b], Anna Zielińska-Jurek [a,*]

[a] Department of Process Engineering and Chemical Technology, Gdansk University of Technology, G. Narutowicza 11/12, 80-233 Gdansk, Poland
[b] Institute for Catalysis, Hokkaido University, N21, W10, Sapporo 001-0021, Japan
[c] Faculty of Chemistry, Jagiellonian University, Gronostajowa 2, 30-387 Kraków, Poland
[d] Department of Solid State Physics, Gdansk University of Technology, G. Narutowicza 11/12, 80-233 Gdansk, Poland
[e] Szewalski Institute of Fluid-Flow Machinery, Polish Academy of Sciences, Fiszera 14, Gdansk, Poland

ARTICLE INFO

Keywords:
Anatase
Doping
Electron trapping
Crystal facets
Reduction

ABSTRACT

Anatase nanoparticles, exposing the majority of the {0 0 1}, {1 0 0} and {1 0 1} facets were synthesized and doped with different niobium amount to investigate the self-trapping of the excess electrons and resulting photocatalytic activity. Photocatalyst structure and presence of excess electrons inside the obtained Nb-doped anatase samples was confirmed by the combination of structural and spectroscopic analyses. Only for the {1 0 1} facets, introduced electrons were found to localize on the surface titanium sites, as long as the analysis was performed in the ambient environment. The photocatalytic activity data, studied in the reaction of 4-nitrophenol reduction and phenol oxidation, show that the dopant-introduced electrons might increase photocatalytic activity only for the anatase structures exposing {0 0 1} and {1 0 0} facets. Ultimately, the dopant effect on the photocatalytic activity depends on the exposed facet, which might be investigated for other systems to increase their applicability.

1. Introduction

Semiconductor-based technologies, such as the photocatalytic degradation process, are one of the most important areas of science and technology with a wide range of possible applications. An induced photoexcitation of an electron from the valence band to the conduction band of a semiconductor material can be seen as a mutual starting point for any further physicochemical phenomena. However, the post-excitation fate of charge carriers often defines the efficiency of a specific process. Focusing on the photocatalytic reactions, their occurrence is directly dependent on the charge transfer between the excited photocatalyst and reacting species present in a medium. This transfer is specifically a surface process, and therefore, the differences in the reaction rate might depend on the atoms' arrangement at the interface. This problem was the subject of numerous studies presented in recent years [1–18], which have both predicted and proved the significance of the photocatalyst surface structure on the efficiency of the photocatalytic reactions. Especially, the preferential localization of photogenerated holes and electrons on the outmost atoms has been deeply analyzed by computational methods [19–24]. The recent studies described in detail the self-trapping phenomena of both charge carriers on a variety of possible TiO_2 surfaces. However, some concerns remain in the interpretation of the reported results. First of all, there is no consensus on the possible surface trapping of the electrons for the low-index anatase facets. Initially, Ma et al. had reported that e^- should be trapped on the (1 0 1) and (1 0 0) surfaces [19], but further study by Carey and McKenna showed that such trapping could occur only for the high index surfaces, such as (1 0 3), (1 0 5) or (1 0 7) [20]. Furthermore, Selcuk and Selloni presented a more detailed analysis, in which it was found that the experimental conditions influence trapping, i.e., electrons are not trapped on the (1 0 1) surface when analyzed in vacuum, but electron trapping occurs when experiments are performed in the presence of water at the interface [21]. It should be pointed out that photocatalytic processes are not performed in a vacuum, and thus, the last finding might be especially important. Nevertheless, experimental verification is still important to discuss these predictions. The other problem with strict interpretation of these studies is that the e^- and h^+ are usually modelled by arbitrarily introducing or withdrawing excess

* Corresponding authors.
E-mail addresses: dudziakszy@gmail.com (S. Dudziak), annjurek@pg.edu.pl (A. Zielińska-Jurek).

https://doi.org/10.1016/j.apcatb.2023.122448
Received 27 September 2022; Received in revised form 30 January 2023; Accepted 8 February 2023
Available online 10 February 2023

electrons from the model. Although obtained results are still useful, closely representing the energy states of the photogenerated charge carriers, this is different from the actual photocatalytic reaction where both e^- and h^+ are generated simultaneously. On the other hand, this is similar to the case of modified semiconductor structure, where point defects should result in a change of the charge carriers number at the ground state. At present, doping of the TiO_2 structure with both metals and non-metals is constantly studied as one of the methods to increase its light absorption properties [25–31]. However, these studies usually do not discuss the dopant effect on the charge carriers' density and how they behave on the surface, while theoretical findings predict that surface dependence could also be expected in that case.

In this regard, the study on the interplay between electron-donating dopant and the surface structure of the anatase TiO_2 photocatalyst is especially desired. First of all, it might help to confirm the possible electron trapping on the commonly observed crystal facets, {0 0 1}, {1 0 0} and {1 0 1}, which might be questionable due to some conflicting results presented in the computational studies. Moreover, verifying the surface-dependent effect of the dopant for TiO_2 would imply that similar behavior might be expected for other photocatalysts and dopants. Therefore, it would define a new approach to the problem of photocatalyst doping in general. Finally, it would be helpful to evaluate how possible surface trapping affects the photocatalytic activity of the prepared materials since the available simulations do not predict it directly.

In view of this, a shallow donor introduced to the anatase lattice is desired to avoid the creation of the deep-trapping states of the dopant. For the anatase TiO_2, Nb can be beneficial as a donor since its shallow character is well-defined, and niobium can be easily incorporated into the anatase structure. Wang et al. reported the introduction of 20 % Nb into the TiO_2 structure without the formation of any secondary phase and only with a limited effect on their absorption properties [32]. The previous studies also predict that for the bulk anatase, a relatively low amount of Nb substituting Ti should not form any additional energy levels [33–36]. Finally, Nb was an element introduced to the anatase models, analyzed by Selcuk and Selloni [21].

In this regard, in the present study, well-defined anatase nanoparticles exposing the majority of the {0 0 1}, {1 0 0} and {1 0 1} facets were prepared and further doped with a low amount of Nb (designed Ti/Nb atomic ratios were 0.5 %, 1.0 % and 1.5 % for each structure) to study the effect of excess electrons on the photocatalytic oxidation of phenol and photoreduction of 4-nitrophenol to 4-aminophenol under simulated solar light. Performed syntheses were based on the reported HF-mediated stabilization of the {0 0 1} facets, as well as pH-controlled growth of the {1 0 0} and {1 0 1} structures via two-step etching-rebuilding process in alkaline conditions [37–39].

2. Experimental

2.1. Preparation of the photocatalysts

Nb-doped anatase nanoparticles with dominant {1 0 1}, {1 0 0} and {0 0 1} exposed facets were prepared hydrothermally. In this regard, commercial TiO_2 P25 (Evonik), potassium hydroxide, sodium hydroxide, 25 % ammonia solution, ammonium chloride, titanium tert-butoxide, n-butanol, 45 % hydrofluoric acid, and niobium(V) ethoxide were used as received. Each nanostructure was synthesized in its non-doped form, as well as with designed Nb contents of 0.5 %, 1.0 %, and 1.5 %, calculated as an atomic percent relative to Ti.

For the synthesis of {1 0 1} exposing nanoparticles, 1 g of TiO_2 P25 was treated with 40 cm^3 of 8.5 M potassium hydroxide solution for the 16 h at the temperature of 200 °C in a 100 cm^3 Teflon-lined autoclave. To obtain desired doping concentration, a corresponding amount of niobium(V) ethoxide was added to the reaction suspension prior to thermal treatment. The obtained products were centrifuged, washed with water to the neutral pH, and dried at 80 °C. Subsequently, 0.4 g of each precursor was further converted to TiO_2 using 100 cm^3 of NH_4OH/NH_4Cl buffer adjusted to pH = 9 (0.3/0.3 M) inside the 200 cm^3 Teflon-lined autoclave at the 210 °C for 16 h. The final products were centrifuged, washed with water five times, and dried at 80 °C.

Synthesis of the {1 0 0} exposing nanoparticles was carried out analogically to the {1 0 1} ones, except that 10 M sodium hydroxide solution was used and the first step was carried out at 120 °C for 24 h. Obtained products were washed with water to the pH of about 10.5 and treated in a Teflon-lined autoclave with 120 cm^3 of pure water at 200 °C for 24 h.

Synthesis of the {0 0 1} exposing nanoparticles was performed in one step, starting from the 17 cm^3 of titanium tert-butoxide, mixed with 30 cm^3 of n-butanol, 3.4 cm^3 of HF solution, and a corresponding amount of niobium(V) ethoxide. The mixtures were kept in the 200 cm^3 Teflon-lined autoclave at 180 °C for 18 h. Obtained products were centrifuged and washed three times with ethanol and further with water as well as 2.5 % NH_4OH solution to obtain neutral pH. After the pH correction, obtained materials were washed with pure water five times and finally dried at 80 °C.

2.2. Phase structure, morphology and elemental composition

The phase structure of the obtained materials was analyzed with the powder X-ray diffraction (XRD) method, using Rigaku MiniFlex 600 instrument. The scan speed during the measurements was $0.75^\circ \bullet min^{-1}$ with the step of 0.05°. Rietveld refinement of obtained patterns was performed using PANanalytical X'Per HighScore Plus 2006 software, based on the Crystallography Open Database data of anatase crystal structure [40]. Profile fitting was based on the pseudo-Voigt function. Specimen displacement, coefficients for background function, lattice parameters *a* and *c*, as well as profile parameters including anisotropic peak broadening were refined. The morphology and elemental composition of the materials were analyzed using FEI Quanta FEG 250 scanning electron microscope (SEM), combined with an Apollo-X SDD energy-dispersive spectrometer (EDS). The EDS data was obtained using accelerating voltage of 30 kV with a scanning resolution of 132 eV and the composition was determined as the average over the large sample area (approx. 2000–4000 μm^2, depending on the samples). Detection level for the analyzed elements, except of oxygen, was determined as 0.1 at %. Obtained data was analyzed using the EDAX Genesis APEX 2i software. Additional elemental analysis was performed for the selected samples using inductively coupled plasma optical emission spectroscopy method (ICP-OES) for the titanium and niobium presence. Development of the surface area for the obtained samples was analyzed with the Brunauer-Emmett-Teller adsorption isotherm method (BET), measured at the 10 points with the N_2 sorption within the p/p_0 range between 0.05 and 0.98 and at the 77.15 K temperature, using Micromeritics Gemini V instrument. Prior to the BET measurements, all samples were degassed at 200 °C for 2 h under the N_2 flow.

2.3. Spectroscopic analyses

The optical absorption of the obtained samples was analyzed via diffuse reflectance spectroscopy (DR/UV–vis) using the Thermo Fisher Scientific Evolution 220 spectrophotometer. Prior to measurements, $BaSO_4$ was used as a reference material in the wavelength range between 190 and 1100 nm. Electron paramagnetic spectroscopy analysis (EPR) was performed at the temperature of liquid N_2, using a Radiopan SE/X-2547 spectrometer with a frequency in the range between 8.911490 and 8.91494 GHz. Modulation amplitude was 5 Gs, for the samples of the {0 0 1} and {1 0 0} series, and 10 Gs for the {1 0 1} ones. The surface properties were analyzed by X-ray photoelectron spectroscopy (XPS, JEOL, JP-9010MC) for 50 scans to estimate the oxidation state of titanium, oxygen and niobium. For the estimation of energy distribution of the electron traps, the photoacoustic spectroscopy (PAS) and reversed double beam photoacoustic spectroscopy (RDB-PAS) with a laboratory-made equipment was performed, as described in the previous paper

[41].

Optical properties of the photocatalyst suspension in water and methanol were performed based on the procedure proposed by Cabrera et al. [42] Briefly, transmittance and diffusive transmittance measurements for the suspensions of the non-modified samples were performed with powder concentration up to 1 g•dm^{-3} in the spectral range of 300–40 nm. Then, specific mass extinction (β) and absorption (κ) coefficients were determined as the slope of the change in the linear region of this relation. The final values are determined as spectral-average and were used to determine mass scattering coefficient (σ), using relation $\beta = \sigma + \kappa$, as well as scattering albedo $\omega = \sigma \bullet \beta^{-1}$.

2.4. Photocatalytic activity tests

Obtained materials were studied in two different photocatalytic reactions: photooxidation of phenol in water and photoreduction of 4-nitrophenol to 4-aminophenol in methanol. All reactions were performed inside the same glass reactor with a quartz window for the light entry, working volume of 25 cm^3, equipped with a magnetic stirrer, cooling jacket and additional hoses for the samples collection and possible introduction of the airflow. The reactor is approximately 3.6 cm in diameter and 2.5 cm thick. For each reaction, prepared photocatalyst suspension was stabilized for 30 or 20 min (details in Table 1) and was immediately introduced to the beam of concentrated 300 W Xe lamp light. During all experiments, reactor position in the light beam was monitored to always be in the centre of the light's intensity, perpendicular to the beam. The measured maximum of the UVA flux intensity at the reactor border was set to be 30 ± 1 mW•cm^{-2} and was controlled directly before and after the reaction. Shimadzu high-pressure liquid chromatography system, equipped with a diode array detector and C18 column (Phenomenex), was used to detect dissolved products (HPLC-DAD). Quantitative analyses, including phenol, para-hydroxyphenol, ortho-hydroxyphenol, benzoquinone, 4-nitrophenol, and 4-aminophenol, were performed after calibration with standard compounds provided by Merck. Summation and some further details on each reaction are presented in Table 1. The detailed scheme, dimensions of the setup, emission spectrum of the utilized xenon lamp and approximate distribution of the light's intensity over the reactor area are presented in Supporting Information (SI). Based on these data, molar flux of photon possible to excite photocatalyst was calculated and compared to the reaction efficiency to achieve apparent quantum efficiency. During these calculations, 6 electrons (6 photons) are needed to reduce one molecule of 4-nitrophenol, while every photon is assumed to possibly induce transformation of phenol. However, since phenol degradation is a step-by-step process, which will include reactions with the formed by-products in the further parts of the process, only an initial rate (5 min) was taken for the calculations.

3. Results and discussion

3.1. Morphology, crystal structure, and composition of the photocatalysts

Morphologies of the synthesized nanocrystals and Nb presence were confirmed by SEM observations and EDS elemental analysis, respectively. As presented in Fig. 1, unique morphology is obtained for each series with only slight impact of the Nb presence on the size of the formed particles.

Furthermore, the shapes of the TiO_2 nanocrystals with exposed facets can be identified based on the Wulff construction of anatase [43]. As presented in Fig. 1a and b, despite the formation of fine nanoparticles, their platelet character can be noticed, which is in accordance with the expected exposition of the {0 0 1} facets. The stabilization of these facet results from the HF presence, as already reported [44–47]. The four elongated sides of the rectangular rods, presented in Fig. 1c and d, correspond to the {1 0 0} facet, which is further topped off with other crystal facets. Finally, octahedral particles, shown in Fig. 1e and f, are almost exclusively enclosed by the {1 0 1} facets, with observed angles between specific crystal sides being very close to the theoretical values (136.6° and 43.4° for the obtuse and the acute ones, respectively). The formation of particles exposing {1 0 0} and {1 0 1} facets depends on the pH value during the second stage of the process, and is directly controlled by the selection of the etching agent (NaOH or KOH), as well as the washing of the obtained precursor and buffer introduction. For these samples, stabilization of both desired facets resulted from the increased alkaline conditions, hydration and oxygenation of the surface [37,48]. Moreover, no clear evidence of other particles than titania (e.g., deposited on the surface of faceted anatase) suggests that secondary phase (e.g., niobium oxide) has not been formed.

Furthermore, EDS analysis confirmed Nb presence in all modified samples, with Nb/Ti ratio consequently increasing with an increase in niobium content during synthesis. The introduction of Nb results from either direct co-crystallization of Ti and Nb from organic precursors or Nb crystallization and diffusion during the two-step etching and rebuilding of the TiO_2 structure [49]. These results are consistent with the additional ICP-OES analysis, however the latter have shown Nb concentrations closer to designed ones for samples from the {0 0 1} and {1 0 1} series. This suggests that for these nanostructures, some preference for Nb to localise near surface might exist, which might influence EDS results. In addition, EDS analysis indicates some differences in the stoichiometry of the prepared samples, which correlates well with the accepted preparation procedures. The {0 0 1} series, synthesized in the H^+ rich environment of n-butanol, is slightly deficient in oxygen, whereas {1 0 0} and {1 0 1} series, prepared in the OH^- rich water solutions, showed no clear signs of O deficiency, when taking into account possible analysis error.

Finally, since slight differences in the size of the particles are observed during SEM analysis, additional measurements of the specific surface area (SSA) were performed. However, no dependence of the SSA on the Nb amount for the prepared samples was noticed. Detailed results of the elemental composition and BET surface area analysis are presented in Table 2.

Furthermore, XRD analysis confirmed that all obtained materials were composed of pure anatase, without any additional crystalline phases, as shown in Fig. 2a. Nevertheless, some differences in the XRD patterns between series are noticeable, especially for samples with exposed {0 0 1} facets. It is known that the morphology of the nanocrystals can affect the width and intensity of the specific XRD reflections and for this series, broadening of the (0 0 4) and (1 0 5) signals at 2θ

Table 1
Details of the performed photocatalytic tests and analytical procedures.

Reaction	Light source and UVA flux int. (mW•cm^{-2})	Setup details	Pre-treatment	Detection method	Mobile phase (volume %)
Phenol degradation	Xe lamp, 30 ± 1	0.2 mM solution, 25 cm^3 reactor, 20 ± 1 °C, 4 dm^3•h^{-1} airflow, in water	30 min stabilization	HPLC-DAD	Acetonitrile – 70 Water – 29.5 H_3PO_4[a] – 0.5
4-nitrophenol reduction		0.5 mM solution, 25 cm^3 reactor, 20 ± 1 °C, in methanol	20 min purging with Ar		Acetonitrile – 39.5 Water – 60 H_3PO_4[a] – 0.5

[a] *given fraction corresponds to the 85 % solution (w/w).*

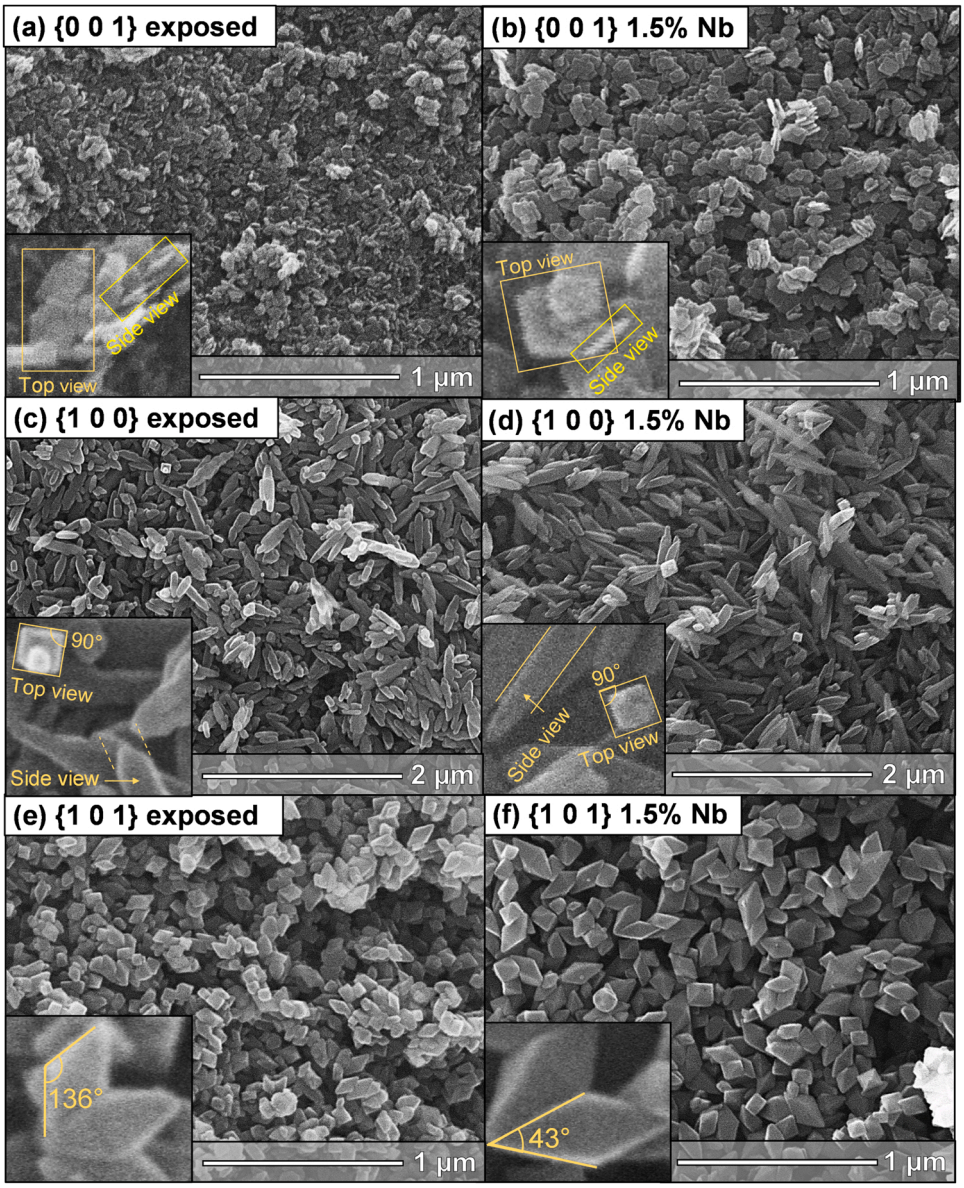

Fig. 1. SEM images of the obtained bare and 1.5 % Nb-modified samples for each series. For images a,b,c and d the "top" and "side" correspond to the views along with and perpendicular to the [0 0 1] crystallographic direction, respectively.

≈ 37° and 54° is in agreement with expected size reduction along with the [0 0 1] crystallographic direction [50]. Therefore, dominant exposition of the {0 0 1} facet can be proven, based on both their morphology and broadening of these reflections. For other series, similar behavior is not observed and XRD patterns resemble typical anatase standard. Nevertheless, an overall consistency of XRD patterns within each series can be noticed, proving that introduced Nb did not influence the crystallization process of the final nanoparticles, which also in accordance with the SEM morphologies. Noteworthy, for the largest content of Nb (1.5 % at.), the possible mass fraction of Nb_2O_5 could reach ca. 3–4 %, and thus it should be relatively high to be detected by XRD. In this regard, it might be proposed that the successful Nb doping is more probable rather than the formation of the heterojunction between TiO_2 and NbO_x secondary phase.

The detailed effect of the Nb introduction on the crystal structure of each nanostructure was further examined including Rietveld refinement of the obtained patterns. Exemplary refined profiles are shown in Fig. 2b for the 1.5 % Nb modified samples, while detailed data is presented in Tables S1 and S2, as well as in Fig. S3 in the Supporting Information. As seen in Fig. 3a, for the {1 0 0} and {1 0 1} series increase of the niobium content linearly increase volume of the unit cell, which is also in accordance with the data reported for the other Nb-doped TiO_2 structures, [51–53]. This change is in a good accordance with possible substitution of Ti^{4+} by a slightly larger Nb^{5+}. Only in case of the {0 0 1} samples, the effect is not linear and generally does not follow any strict order. This might be especially due to some amount of O deficiency, which was suggested by the EDS results and could be expected due to the aggressive HF environment used during the synthesis [54]. Therefore, in this particular series, slight amount of O vacancies might also form along the Nb presence, which results in a “chaotic” evolution of the unit cell volume. Finally, calcination of the samples modified with 1.5 % Nb in each series at 600 °C for 2 h have not shown crystallization of any Nb phase, which suggest that no amorphous Nb species are present [55]. Noteworthy, this process also induce expansion of the unit cell in case of the {1 0 1} {1 0 0} samples and contraction in case of {0 0 1} one, as shown in Fig. 3b. These facts will be discussed in the further parts.

Table 2
Summation of the EDS, ICP-OES and BET surface area analysis for all samples.

Sample name	Designed Nb/Ti (at.)	EDS Nb/Ti (at.)	ICP-OES Nb/Ti (at.)	EDS O/Ti (at.)	BET surface area ($m^2 \bullet g^{-1}$)
{0 0 1}	0	0	n.d.	1.8 ± 0.50	84
{0 0 1} 0.5 % Nb	0.005	0.003 ± 0.002	0.0057 ± 0.0010	2.0 ± 0.50	79
{0 0 1} 1.0 % Nb	0.010	0.009 ± 0.002	n.d.	1.7 ± 0.50	81
{0 0 1} 1.5 % Nb	0.015	0.011 ± 0.002	0.0177 ± 0.0010	1.8 ± 0.50	92
{1 0 0}	0	0	n.d.	1.9 ± 0.50	17
{1 0 0} 0.5 % Nb	0.005	0.005 ± 0.002	0.0048 ± 0.0010	3.0 ± 0.50	16
{1 0 0} 1.0 % Nb	0.010	0.008 ± 0.002	0.0081 ± 0.0010	2.3 ± 0.50	14
{1 0 0} 1.5 % Nb	0.015	0.013 ± 0.002	n.d.	2.7 ± 0.50	16
{1 0 1}	0	0	n.d.	1.9 ± 0.50	23
{1 0 1} 0.5 % Nb	0.005	0.003 ± 0.002	n.d.	2.2 ± 0.50	15
{1 0 1} 1.0 % Nb	0.010	0.005 ± 0.002	0.0110 ± 0.0010	2.3 ± 0.50	14
{1 0 1} 1.5 % Nb	0.015	0.011 ± 0.002	n.d.	2.3 ± 0.50	16

3.2. XPS and DR/UV–vis spectroscopy

To study the surface composition and oxidation state of elements, XPS analyses were performed and obtained data are summarized in Table 3, as well as exemplary spectra are presented in Fig. 4. For the {0 0 1} and {1 0 1} samples, niobium content correlates with used precursor, i.e., the higher the Nb amount used for the synthesis was, the higher was its content in the resultant samples, reaching 1.5 %, 2.5 % and 3.2–3.6 % (in respect to titanium) for 0.5, 1.0 and 1.5 samples, respectively. These data indicate the enrichment of {1 0 1} and {0 0 1} surfaces with niobium, which is also in accordance with the comparison of EDS and ICP-OES results. Thus, some preference for surface modification rather than uniform bulk doping is expected for these samples. However, in the case of {1 0 0} sample, an increase in niobium content does not result in an increase in its content on the surface. Moreover, a decrease in niobium content from 2.1 % to 1.0 % and 0.05 % (for 0.5, 1.0 and 1.5 samples, respectively) has been observed, which means that either there is some limit of titania "doping/modification" with niobium (at ca. 0.5 at %) or niobium is mainly doped in the bulk. Similar doping limits have already been reported for other materials, e.g., Rh-doped titania [56]. However, the former does not explain a decrease in niobium content, and thus Nb-doping in the bulk is rather proposed for {1 0 0}-based samples All samples are highly enriched with oxygen on the surface, where oxygen to titanium ratio exceeds stoichiometric 2.0, reaching even ca. 4.0, which is typical for titania sample, being caused by the presence of hydroxyl groups and adsorbed water. Interestingly, the modification of samples with niobium causes different effect, i.e., an increase and a decrease in oxygen content. In contrast, in the case of titania modification with deposits of noble, rare-earth metals and ruthenium complexes, a decrease in oxygen content has been commonly observed, resulting from the replacement of hydroxyl groups by metal, and thus even lower O/Ti ratio than 2.0 [57]. Here, lack of strict correlation between low O/Ti ratio and niobium content suggest that similar -OH replacement is not occurring and Ti-Nb bonds probably do not form. This is also in agreement with the used Nb precursor (ethoxide), which already introduced oxidized Nb form with attached oxygens.

Titanium, oxygen and niobium peaks have been deconvoluted, as exemplary shown in Fig. 4. Titanium exists mainly in Ti^{4+} form as it is in TiO_2, but slight content of reduced Ti^{3+} was also noticed, which is typical for various titania samples. For example, for O/Ti ratio data, there is no clear correlation between niobium amount and the content of Ti^{3+}. On the contrary, niobium exists mainly in four-valence state, reaching 72–96 %. This could suggest the formation of the fine NbO_2 on the surface, however reduction of the Nb^{5+} to Nb^{4+} during the synthesis procedure is not expected, as well as the presence of stable NbO_2 will not be supported by the UV–vis analysis, especially for the {0 0 1} and {1 0 0} samples. On the other hand, it is known that Nb competes with the Ti as the trapping site for excess electrons when considered as a dopant and the localization of the charge on Ti is specifically stabilized by the environment [21]. In this regard, under the XPS vacuum conditions, a preference to trap electrons on the Nb might be expected, which causes its reduction to Nb^{4+}. Nevertheless, the minority of the Nb^{5+} states is also always present, with no clear correlation with the amount of introduced Nb. This suggests that some competition between Nb doping and the formation of other Nb structures (e.g. oxides) might still happen, however the latter seems to be limited.

Furthermore, the XPS studies were followed by the DR/UV–vis absorbance analysis. The effect of the photocatalyst morphology can be observed, with {1 0 1} enclosed anatase particles exhibiting a significant absorption increase in the Vis and NIR regions (see in Fig. 5). Similar, but much smaller effect is also observed for the {0 0 1} samples. Therefore, additional energy states are created within the material, especially for this series.

This effect for the {1 0 1} series cannot originate from the possible Nb_2O_5 presence, since its bandgap is almost the same as that of anatase TiO_2, and no mid-gap states should be visible in the spectrum [58–62]. Furthermore, such effect could result from the presence of the stable NbO_2 phase, but this is not supported by XRD and SEM analysis. Moreover, additional treatment of the 1.5 % Nb sample with H_2O_2 (30 min, with high excess of molar H_2O_2 relative to Ti) resulted in no change in the absorbance as shown in the Fig. S4 in the Supporting Information. Similar effect was also observed for the O_3 treatment. Therefore, formation of any oxidizable species on the surface of this sample cannot be responsible for the formation of these additional states. This includes possible reduced Nb species, as well as surface oxygen vacancies and possible carbon species. Furthermore, the XPS results have shown that Nb^{4+} cations are present in all TiO_2 nanostructures with similar content, which cannot explain differences in the absorbance between the series. In this regard, it is expected that this effect results from different localization of the electrons introduced to the TiO_2 lattice with the Nb dopant, which should depend on both the surface structure and the environment. Especially, transfer of e^- from Nb site to the surface Ti is suggested for the {1 0 1} facets, based on the simulations performed at the interface with water [21]. Therefore, especially for this series, the formation of the Ti^{3+} defects might be preferred under the ambient conditions, which is also in agreement with increased Vis-NIR absorbance. Similar effect is also a well-known phenomenon for the oxygen-deficient TiO_2, which ultimately causes the blue coloration of the powder [63–66]. However, especially in the case of anatase samples exposing {1 0 0} and {1 0 1}, no presence of oxygen vacancies is expected since these samples were prepared in relatively oxygen-rich conditions under high pH values. Moreover, both EDS and XPS measurements have not indicated any oxygen deficiency for these series. The fact that Vis-NIR absorbance of the {1 0 1} is not related to the oxygen vacancies is also in accordance with the performed calcination of the 1.5 % Nb sample, which resulted in the expansion of the unit cell. As the oxygen deficiency results in the formation of Ti^{3+}, the

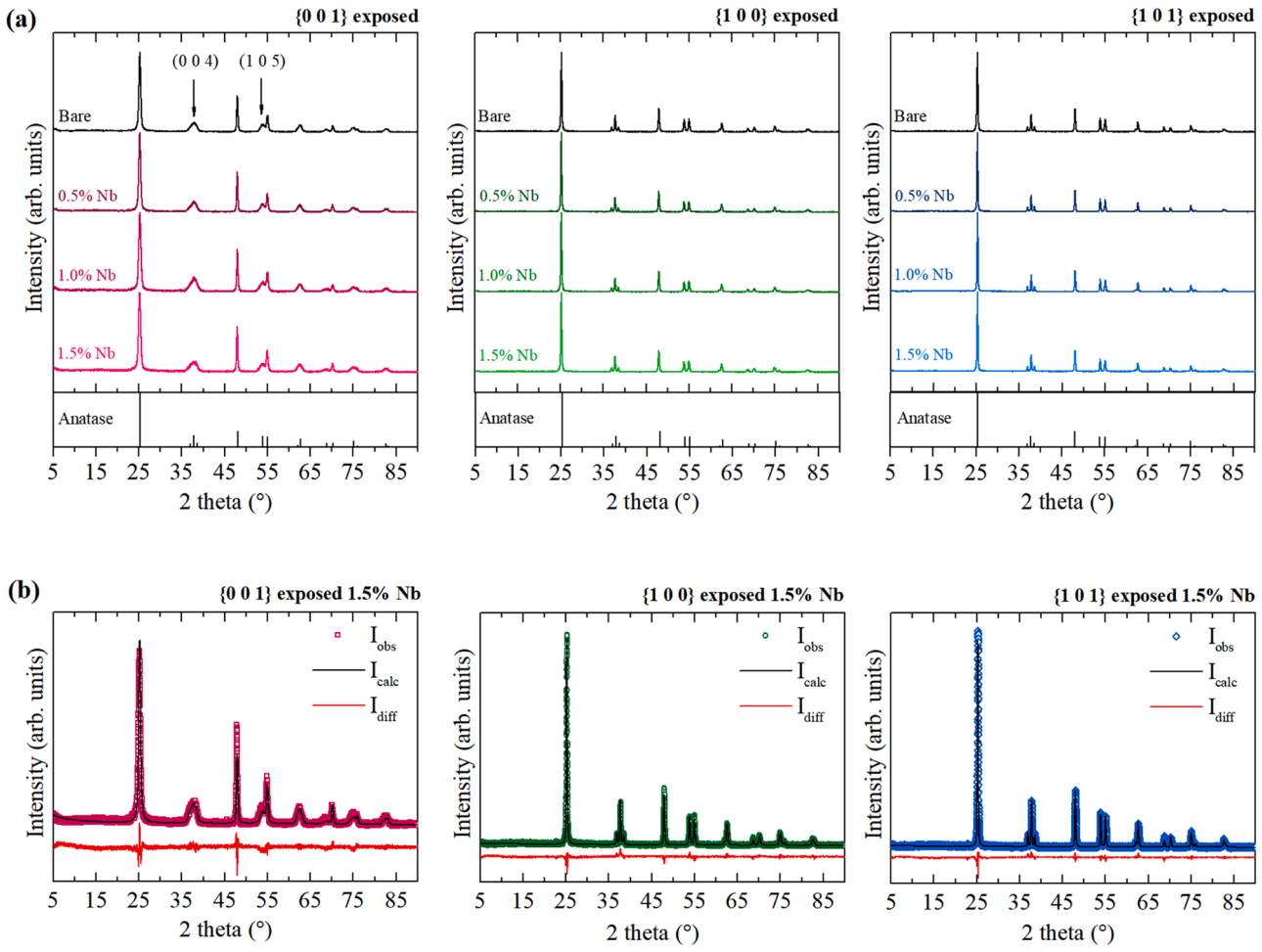

Fig. 2. XRD patterns of the obtained TiO_2 photocatalysts (exposing different crystal facets) modified with Nb (a) and exemplary Rietveld refined patterns for the most modified samples in each series (b).

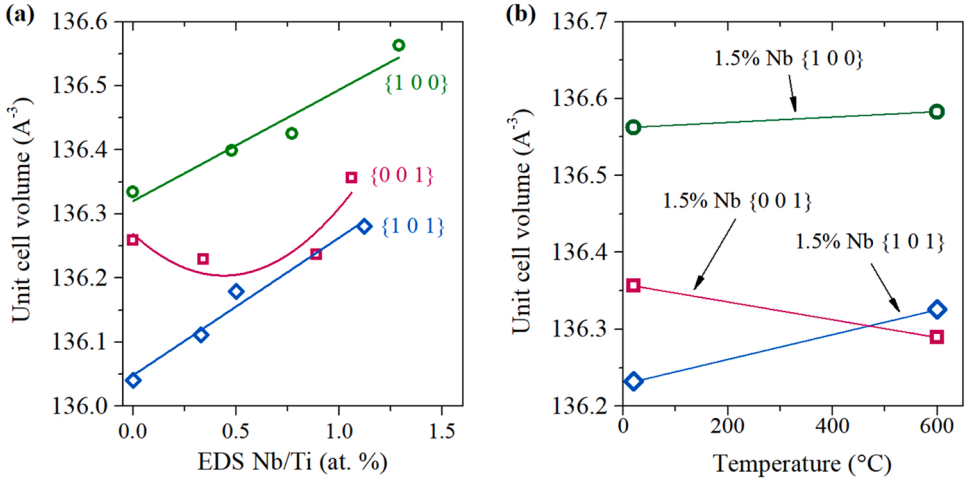

Fig. 3. Effect of Nb presence on the unit cell volume obtained from the refined XRD patterns (a) and calcination effect on the unit cell volume of the most modified sample in each series (b).

unit cell of the reduced TiO_2 is also know to expand similarly to the Nb^{5+} doping [67]. However, in consequence, if vacancies are removed from the structure, contraction might be expected as the source of the excess electrons disappears from the structure. In fact, this is observed for the calcined {0 0 1} 1.5 % Nb sample, where some V_O might be present due to the accepted preparation procedure. In the case of the 1.5 % {1 0 1} the unit cell expands which, interestingly, is also accompanied by the diminishing of the Vis-NIR absorbance, as shown in Fig. S5 in Supporting Information. Instead, a slight new absorbance band appear down to the ~2.4 eV. Noteworthy, such behavior is in a very good agreement with possible incorporation of the excess oxygens into the TiO_2 structure, which can form absorbance states at similar energy levels [35].

Table 3
Summation of the XPS data for the obtained samples.

Sample name	XPS Nb/Ti (at.)	XPS O/Ti (at.)	Ti species (at %)		Nb species (at %)	
			4 +	3 +	5 +	4 +
{0 0 1}	0	3.03	94.3	5.7	-	-
{0 0 1} 0.5 % Nb	0.015	2.35	95.0	5.0	23.9	76.1
{0 0 1} 1.0 % Nb	0.025	4.25	93.7	6.3	3.5	96.5
{0 0 1} 1.5 % Nb	0.036	3.02	93.7	6.3	11.4	88.6
{1 0 0}	0	3.65	95.69	4.3	-	-
{1 0 0} 0.5 % Nb	0.021	3.76	93.3	6.7	28.2	71.8
{1 0 0} 1.0 % Nb	0.010	2.16	95.2	4.8	3.7	96.3
{1 0 0} 1.5 % Nb	0.005	2.34	96.1	3.9	22.6	77.4
{1 0 1}	0	2.30	95.7	4.3	-	-
{1 0 1} 0.5 % Nb	0.015	2.29	95.6	4.4	17.9	82.1
{1 0 1} 1.0 % Nb	0.025	2.33	94.6	5.4	29.5	70.5
{1 0 1} 1.5 % Nb	0.032	2.16	95.9	4.1	7.5	92.4

Moreover, introduction of excess atoms would explain well expansion of the unit cell. Formation of such O rich structure is also in agreement with possible passivation of the Nb-doping, which was discussed in the literature [34,68].

As for the {0 0 1} and {1 0 0} samples, the relatively low absorption suggest that similar electron trapping (on the surface or in the bulk) is less prominent, which indicates that introduced electrons became delocalized over different sites. This is in agreement with the general predictions for the bulk anatase doped with Nb, proving that this phenomenon depends on the surface structure [34–36].

Furthermore, DR/UV–vis analysis could be discussed in terms of the possible formation of O-rich anatase structures for the {1 0 0} series, which might be suggested, since it was characterized by the high O/Ti ration during the EDS analysis and no absorbance increase characteristic for the excess electrons was observed. However, as shown for calcined 1.5 % {1 0 1} sample, combination of Nb and O_I defects inside the anatase crystal structure, as well as Nb with surface peroxo complexes, should create additional energy states above the valence band edge (yellow coloration) [34,68]. This effect was also reported for other point defects related to the oxygen excess inside the TiO_2 structure, such as a simple O excess [69,70], Ti vacancy, or interstitial Ti [30,71]. In this regard, the almost perfect alignment of the absorbance edge for the {1 0 0} samples cannot support the formation of such O-rich structures. Therefore, the high oxygen amount observed for these samples could result from high surface hydroxylation, which might be connected with highly alkaline preparation conditions.

In this regard, DR/UV–vis spectroscopy has revealed possible surface trapping of the Nb-originating excess electrons on the titanium sites of {1 0 1} facets, as predicted by the computational studies. However, since this trapping depends on the interface character and is not preferred in a vacuum, XPS was found to be not reliable in the determination of the possible surface Ti reduction. Instead, excess electrons are preferred to trap on the Nb atoms, causing the appearance of dominant Nb^{4+} signals. Therefore, to further prove the differences between the samples, additional analyses were performed based on the low-temperature EPR and RDB-PAS measurements, as both of these techniques are surface-sensitive and do not require vacuum conditions.

3.3. EPR spectroscopy and RDB-PAS

The EPR spectra of the pure and 1.5 % Nb samples for each series, in which three main signals can be identified, are presented in Fig. 6. The signals located at $g \approx 1.989$ and $g \approx 1.955$ are well-known to originate from the electrons trapped at the bulk Ti sites (bulk Ti^{3+}) and are the only signals observed for the {0 0 1} exposed nanoparticles [72–74]. Moreover, existence of some bulk Ti^{3+} defects in these samples is in agreement with a discussed presence of O vacancies for these nanoparticles. Nevertheless, although precise quantification was not possible during this analysis, a higher signal-to-noise ratio is observed for the 1.5 % Nb-TiO_2 sample, suggesting that a higher number of Ti^{3+} states were formed when Nb was introduced to the photocatalyst, under otherwise identical synthesis conditions. An increase of the bulk Ti^{3+} states is especially connected with excess electrons present inside the TiO_2 lattice, which further prove the doping behavior of the introduced Nb. It could also be noted that both bare and 1.5 % Nb {0 0 1} samples were characterized by almost identical O-stoichiometry both during the EDS and XPS analyses. Furthermore, for other samples, the additional signal at $g \approx 2.003$ is observed, especially for the unmodified structures. The signal in this region is often observed due to the electrons trapped at the oxygen vacancies. However, it is generally observed as a sharp and symmetrical peak in both high and low fields of the spectrum, which is not the case here. Moreover, both EDS and XPS analyses have not revealed any meaningful oxygen deficiency for these series. Therefore, these signals' appearance might be connected with possible charge carriers trapping at the different oxygen species. This might include the formation of the lattice O^-, as well as $\bullet O_2^-$ at the surface since both of these species are characterized by signals with similar g values [75–78]. Although their precise identification seems to be impossible for obtained results, they do not correlate with the observed absorbance increase for the {1 0 1} series, nor the Nb presence. Therefore, it can be assumed that their appearance results from the features specific to each facet type, and they should not contribute to the differences observed within the series. On the other hand, the introduction of Nb further causes the appearance of different features in the spectrum of both {1 0 0} and {1 0 1} samples. For nanoparticles enclosed with the {1 0 0} facets, Nb presence creates additional bulk Ti^{3+} states, similar to the {0 0 1} samples. However, this signal is relatively low compared to the possible $O^-/\bullet O_2^-$ formation, which is dominant for this sample. This is in agreement with the absorption studies, which have shown that the formation of the Ti^{3+} states at room temperature is not observed by the UV–vis spectroscopy. Therefore, their delocalization should be preferred in the room conditions for the {1 0 0} structure. Finally, in the case of the {1 0 1} sample, Nb presence results in the clear distortion of the EPR signal for the $g < 1.99$. The overlapping of the low-intensity signals in this region originates from the electron trapping on the surface Ti sites (surface Ti^{3+}). In this case, the lack of a strictly defined peak results from the differences between the various surface sites, forming a broad distortion-like signal in this region. This behavior is well-observed only in the spectrum of the Nb-modified {1 0 1} sample. Since, in this spectrum, no other high-intensity signals are observed, the formation of the surface Ti^{3+} seems to be the only possible explanation for the combined EPR and DR/UV–vis results, and thus proving the surface trapping of the excess electrons only for the {1 0 1} facets.

Finally, RDB-PAS analysis was performed to obtain the energy distribution of the electron traps within the materials. During these analyses, valence band electrons are excited directly to the trapping sites of the semiconductor using wavelength scanned continuous light irradiation in the presence of methanol as the scavenger of photogenerated holes. This method was designed specifically to investigate photocatalyst powders allowing analysis of their surface traps, identification of the specific materials as well as observing possible interphase charge transfer [79–81]. Fig. 7 shows obtained distributions of trap density for pristine and Nb-doped samples (total densities are given in chevrons). As shown, niobium presence contributed differently to the trap density, depending on the nature of the exposed facets. Especially, for the {1 0 1} samples, systematic reduction of the trapping sites' density is observed together with the increase of the Nb content. As reported before,

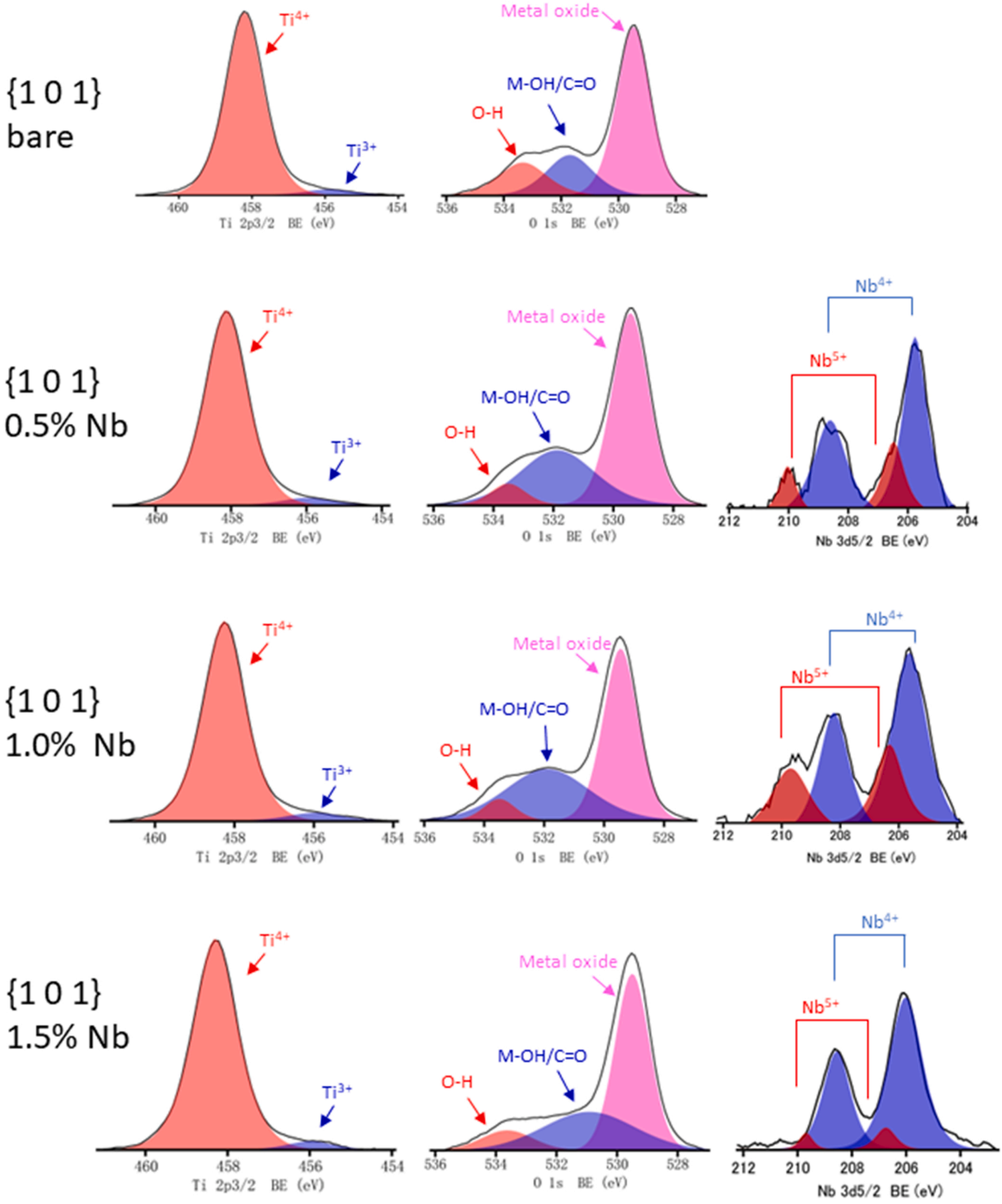

Fig. 4. Exemplary XPS results for {1 0 1} samples of Ti $2p_{3/2}$, O 1 s and Nb $3d_{5/2}$.

RDB-PAS analyses are specifically sensitive towards the surface electron traps, showing a clear trend of the determined trap density, together with the surface area of the photocatalyst [79]. Therefore, a decrease of the trap density for the {1 0 1} samples should especially result from filling of these surface states with excess electrons, introduced together with the Nb. This is not observed for the {0 0 1} and {1 0 0} samples, where Nb presence does not affect total densities in a significant way. This agrees with the EPR results, which showed the appearance of the bulk Ti^{3+} states for these samples, when Nb was introduced. Ultimately, this further proves that only in the case of Nb-doped {1 0 1} samples

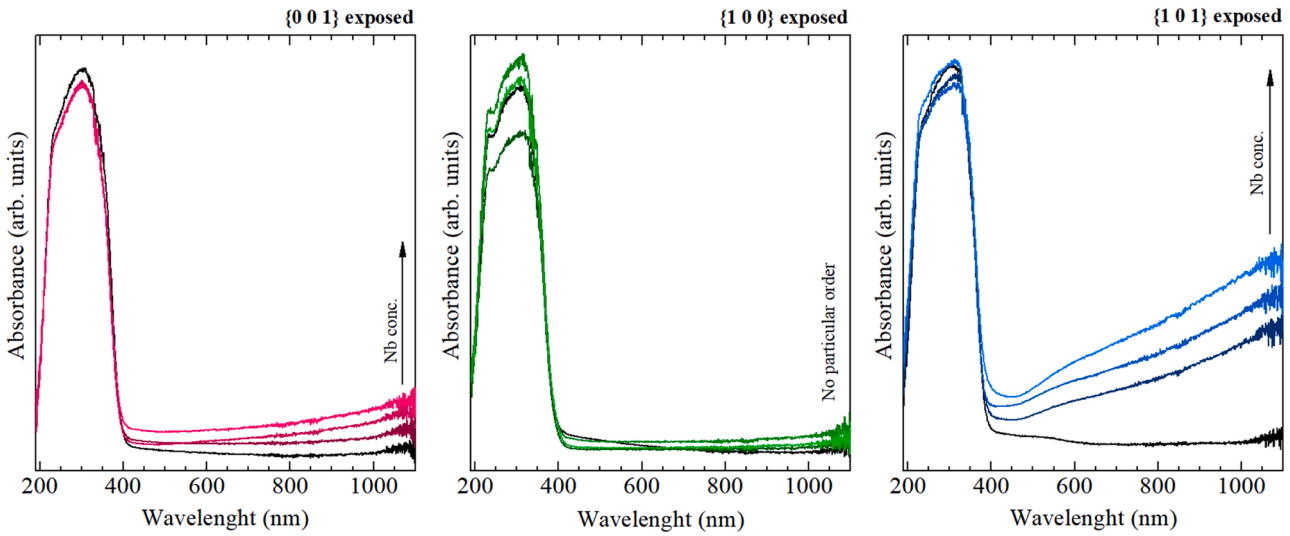

Fig. 5. DR/UV–vis absorption analysis for the obtained TiO_2 photocatalysts doped with Nb and exposed with different crystal facets.

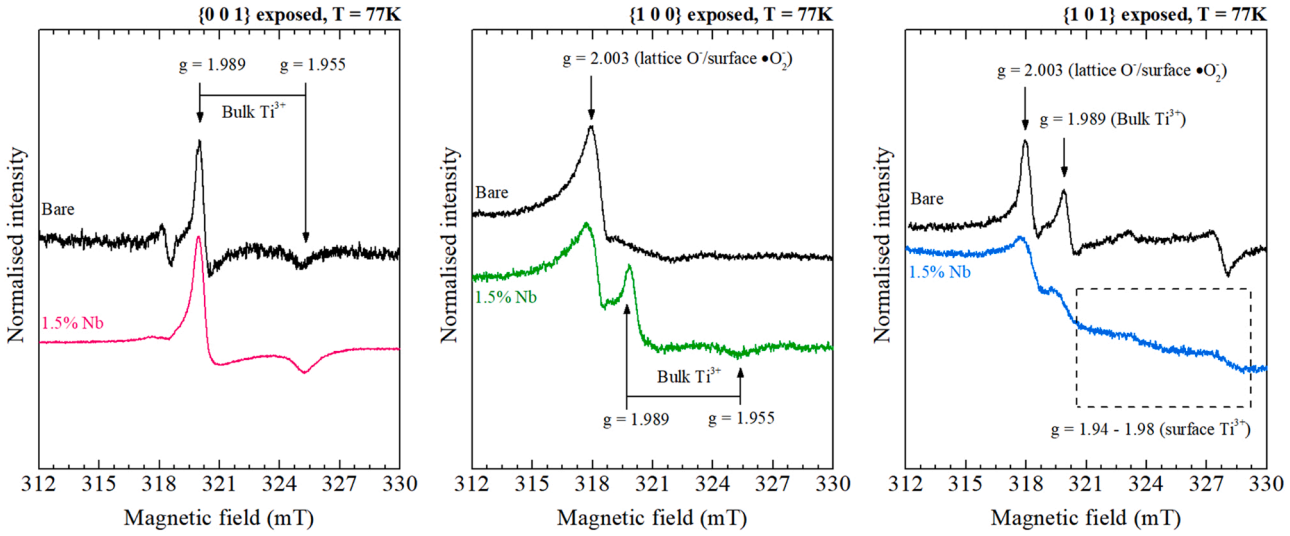

Fig. 6. Low temperature (77 K), min-max normalized EPR spectra of the bare and most Nb-modified TiO_2 samples in each series.

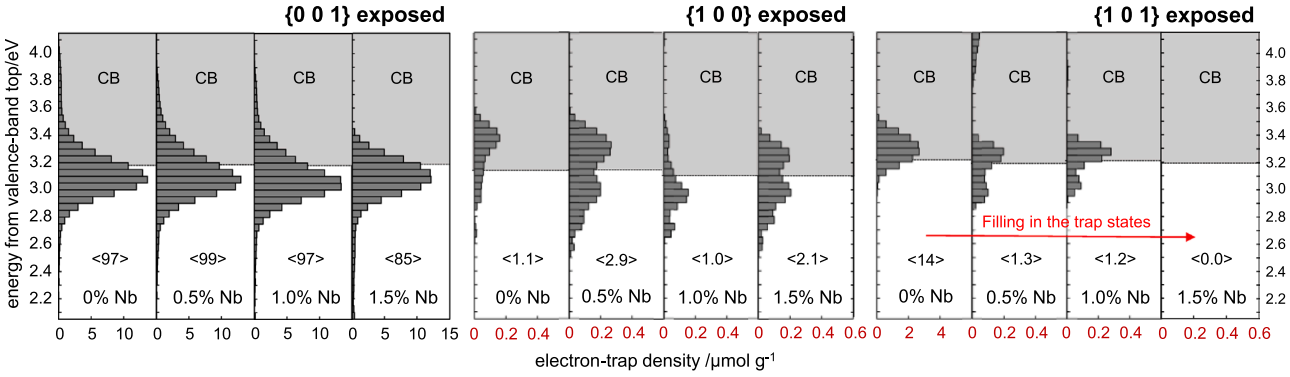

Fig. 7. Energy distributions of the electron trap density present in the prepared TiO_2 samples, as obtained from the RBD-PAS measurements. Total densities are given in chevrons. Please note different X scale between the samples.

additional electrons should trap at the surface sites.

Furthermore, in the case of samples {1 0 0} the density of electron traps is overall very low, which might be due to the preferred hole trapping, reported previously for this surface [19], as well as possible capping of the trapping sites with i.e. -OH groups. The second might be especially reasonable due to the alkaline conditions present during the

synthesis and generally high oxygen presence observed for these series. Similar effect might also be suggested for the {1 0 1} exposing sample, where electron traps might be hypothetically capped with both -OH and ammonia, however further reduction of their density, together with Nb is still noticeable for these samples. Finally, especially for the {1 0 0} facets, the introduction of the Nb promotes the appearance of the additional trapping sites, approx. 0.2 eV below the conduction band edge. This is also observed for the 0.5 % and 1.0 % Nb-modified {1 0 1} samples, however, the effect disappeared together with the reduction of the trapping sites amount. The appearance of these states may result from the formation of the secondary phase inside the photocatalyst, with its valence band edge having lover potential than the primary material. In such a case, electrons from the secondary phase could be excited to the trap states of the primary material with lower energy [81]. The same can result if additional energy states are created above the valence band edge of the anatase. However, especially for the {1 0 0} samples, this is not supported since no difference in the absorption spectra was observed, as well as XPS/EDS analysis revealed that Nb localizes in the bulk of the material for the higher concentrations. On the other hand, a similar maximum of the trap density below the conduction band is always present for the {0 0 1} samples, which are especially characterized by the bulk Ti^{3+} defects. In this regard, for the {1 0 0} structures, these states also appear as a consequence of the increased number of bulk defects, as shown by the EPR analysis.

Ultimately, based on the combined structural, morphological, and spectroscopy analyses, Nb is expected to act as the electron-donating dopant in the prepared anatase TiO_2 samples, which resulted in the presence of excess electrons inside its crystal lattice. The self-trapping of these electrons on the Ti centres could be observed under the non-vacuum conditions, showing their preferred surface localization only for the {1 0 1} facets. These results are in good agreement with some of the computational predictions, simultaneously proving that such trapping can occur for the low-index TiO_2 facets under the ambient conditions [21]. Therefore, similar phenomena might also be expected for the other semiconductor/dopant combinations. It should also be noted that different effects could be expected for the commonly obtained non-faceted, spherical particles, since it is known that charge carriers trapping is different in such structures [23]. Finally, to verify how this self-trapping at the ground states affects the photocatalytic activity of the prepared samples, photoreduction of the 4-nitrophenol, as well as photooxidation of phenol were studied in the presence of the obtained Nb-doped anatase structures.

3.4. Determination of the optimal photocatalyst concentrations

Prior to the actual analysis of the photocatalytic activity, photocatalyst concentration was optimized for both reactions (phenol degradation in water and 4-nitrophenol reduction in methanol) to account for the possible effect of different optical properties of the suspensions. For the phenol degradation, procedure was performed experimentally, following suggested protocol with P25 as an internal standard [82]. As shown in Fig. 8, all samples show a bit different increase of the observed rate constant, however in each case they achieve maximum activity around 2 $g{\cdot}dm^{-3}$, which was adapted as optimal for this reaction.

Furthermore, due to the different environment used, performance might be different in case of 4-nitrophenol reduction. Therefore experimental results of phenol degradation were followed with determination of optical properties for each sample (both in the water and methanol), as specified in the experimental section. Summation of the obtained parameters is shown in Table 4, together with the resulting apparent optical thickness of the reactor, calculated based on the six-flux model (SFM) as $\tau_{app} = \beta{\bullet}C{\bullet}L{\bullet}A{\bullet}(1- \omega_{corr}^2)^{1/2}$ [83], where C is photocatalyst concentration, L is reactor length (2.5 cm), ω_{corr} is corrected scattering albedo and A is SFM parameter [84]. Noteworthy, obtained values are quite consistent with the parameters reported for other TiO_2 materials [85,86], including P25 ($\beta = 14705\ cm^2{\bullet}g^{-1}$, $\kappa = 3088\ cm^2{\bullet}g^{-1}$, $\omega = 0.79$ in water [87]).

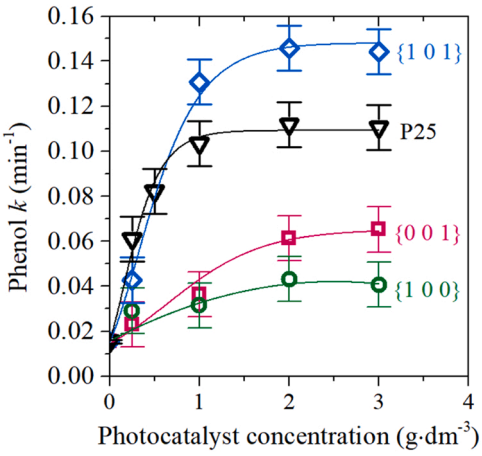

Fig. 8. Change of the observed phenol degradation rate as the function of photocatalyst concentration for each of the unmodified samples and P25 control. Experimental error based on the variance of P25 at the optimal concentration of 2 $g{\bullet}dm^{-3}$. Rate constant determination is presented in Figs. S6 and S8 in Supporting Information.

Based on these calculated parameters two observations can be made. Firstly, the experimentally determined optimal concentrations from Fig. 8 achieve quite larger values of τ_{app}, comparing to the optimal ones reported in the literature (approx. 3–4 [87,88]). In general, as shown in Fig. S7 using P25 as an example, the experimental degradation rate increase slower than photon absorption predicted with SFM. This effect is systematic for all samples, suggesting its dependence on the experimental setup, rather than photocatalyst itself. In this regard, it could be highlighted that the reactor used does not follow some of the SFM assumptions [84]. This includes mostly non-uniform photocatalyst distribution (especially under high concentrations and due to intensive stirring directly inside the reactor space), as well as limited size of the reactor in all directions with significant flux changes at the reactor border (see Figs. S1 and S2b). In this regard, differences between experimental and SFM results seems reasonable, leading to experimentally best conditions at 2 $g{\cdot}dm^{-3}$.

Secondly, the optical properties in methanol are different than in water and are actually similar between all samples. This fits quite well observations by Delforce et al., who have shown that isoelectric point of TiO_2 in methanol is significantly shifted to the basic conditions (approx. pH = 11), compared to the water (close to the neutral conditions) [89]. Therefore, stabilization of the photocatalysts suspension in methanol might be expected due to the relatively strong surface charge regardless of the sample, resulting in a similar optical properties of the suspensions. Furthermore, following calculated τ_{app} it was suggested that optimal conditions for 4-nitrophenol reduction might have been achieved at 1 $g{\cdot}dm^{-3}$, due to the similarities with the results obtained for phenol. However, as shown in Fig. S9 in the SI, further increase of the photocatalyst concentration up to 2 $g{\cdot}dm^{-3}$ resulted in a systematic increase of the reduction efficiency, independently of the optimal τ_{app} observed for water reaction. As this reaction is fundamentally different from phenol degradation, this shown that optimal conditions are probably not the same for these two systems. Nevertheless, the relative differences observed between 1 and 2 $g{\cdot}dm^{-3}$ are similar for all tested samples, which agrees with similar optical properties of methanol suspensions. In this regard, comparison at the same concentration should be reasonable to determine the Nb effect, independently on the strictly optimal conditions. Therefore, results obtained at the 1 $g{\cdot}dm^{-3}$ were taken for further discussion.

Table 4
Summation of the calculated optical properties in water and methanol.

Water					Apparent optical thickness τ_{app}			
Sample	β ($cm^2 \bullet g^{-1}$)	κ ($cm^2 \bullet g^{-1}$)	σ ($cm^2 \bullet g^{-1}$)	ω	0.25 $g \bullet dm^{-3}$	1 $g \bullet dm^{-3}$	2 $g \bullet dm^{-3}$	3 $g \bullet dm^{-3}$
{0 0 1}	38837	9339	29499	0.76	10	39	78	118
{1 0 0}	13011	3545	9466	0.73	3.5	14	28	42
{1 0 1}	11484	3404	8080	0.70	3	13	26	39
Methanol					Apparent optical thickness τ_{app}			
Sample	β ($cm^2 \bullet g^{-1}$)	κ ($cm^2 \bullet g^{-1}$)	σ ($cm^2 \bullet g^{-1}$)	ω	0.25 $g \bullet dm^{-3}$	1 $g \bullet dm^{-3}$	2 $g \bullet dm^{-3}$	3 $g \bullet dm^{-3}$
{0 0 1}	29062	4071	24991	0.86	6	23	46	68
{1 0 0}	30352	5517	24836	0.82	7	27	53	80
{1 0 1}	27706	5996	21710	0.78	7	27	53	80

3.5. Photocatalytic activity

The effect of Nb-introduced excess electrons in anatase structure with exposed different crystal facets on photocatalytic reduction of 4-nitrophenol to 4-aminophenol in methanol is presented in Fig. 9, while detailed kinetics are presented in Supporting Information. Moreover, selectivity of the reduction process was calculated as the ratio between produced 4-aminophenol and the number of disappeared 4-nitrophenol molecules (mean over time). From these results, a clear effect of the exposed facet, as well as Nb presence, can be observed. For the bare TiO_2 materials, both directly observed and per-surface reduction activity order is {1 0 1} > {0 0 1} > {1 0 0}, which is in agreement with preferred photoreduction character of these surfaces [19]. Furthermore, for the {1 0 1} samples introduction of the Nb resulted in visible decrease in their reduction ability, although excess electrons localize on the surface and the calculated selectivity was significantly increased for this series. This decrease is observed independently of the surface normalization and is linear after normalization. In this regard, the introduction of the additional electrons could not support the reduction ability of the {1 0 1} facets. This might result from two possible effects. Firstly, a significant amount of surface defects, such as Ti^{3+}, might increase the recombination rate at the surface, therefore decreasing the total amount of reacting charge carriers for these structures. Secondly, it might be expected that a large number of excess electrons localized on the surface would inhibit the photooxidation reaction, which must also occur to counter the reduction process. In such a case, the process might start to be limited by lowering the photooxidation potential of these materials. On the other hand, both for the {0 0 1} and {1 0 0} samples, the introduction of the Nb increased their reduction ability, with some maximum observed somewhere up to the ~0.7 at % of Nb/Ti ratio. Again, the Nb effect is observed both without and after considering possible effect of the surface development. Noteworthy, for the modified structures, the {0 0 1} samples achieve the highest reduction ability as a combination of positive Nb effect and high surface area. Furthermore, from the three investigated facets, only the {1 0 1} ones are expected to preferably trap electrons over the photogenerated holes [19]. In this regard, positive Nb effect also correlates with the "oxidative" character of both {0 0 1} and {1 0 0} surfaces. For the surface-normalized results, the highest increase of the reduction ability is observed for the {1 0 0} series, which would create precisely opposite trend to the reduction ability of the non-modified facets (highest increase for the most oxidative facet and a decrease for a reductive one). However, it must be noted that the exact relation between the surface development of the specific facet and observed nitrophenol reduction is not proved so far, therefore it is not obvious if activity would increase linearly with the photocatalyst surface area. In this regard, such observation would need further investigation. On the other hand, for the non-normalized results, the highest reduction enhancement by Nb presence is observed for the {0 0 1} facets, which would also correlate with the highest electron trap density. For both {0 0 1} and {1 0 0} samples Nb presence increase reduction selectivity, the same as for the {1 0 1}, however the effect is visibly lower for the {0 0 1} ones.

Furthermore, degradation of phenolic compounds occurs through photogenerated reactive oxygen species, which are created through reduction and oxidation reactions [90]. As shown in Fig. 10, the effect of the exposed facet and Nb presence can also be noticed, especially for the {1 0 1} samples, however differences are less noticeable than for nitrophenol reduction. The per-surface activity for the bare anatase

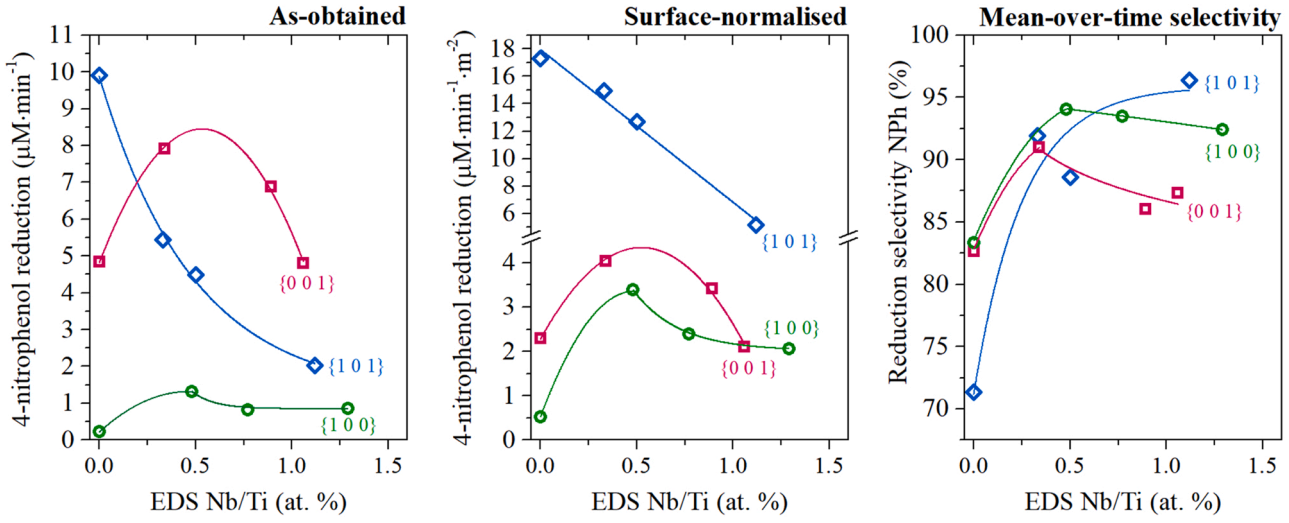

Fig. 9. As-obtained and surface-normalized efficiency of the photocatalytic 4-nitrophenol reduction to 4-aminophenol after a 30 min process, together with the calculated selectivity as the function of exposed crystal facet and Nb concentration. Lines are added as guides.

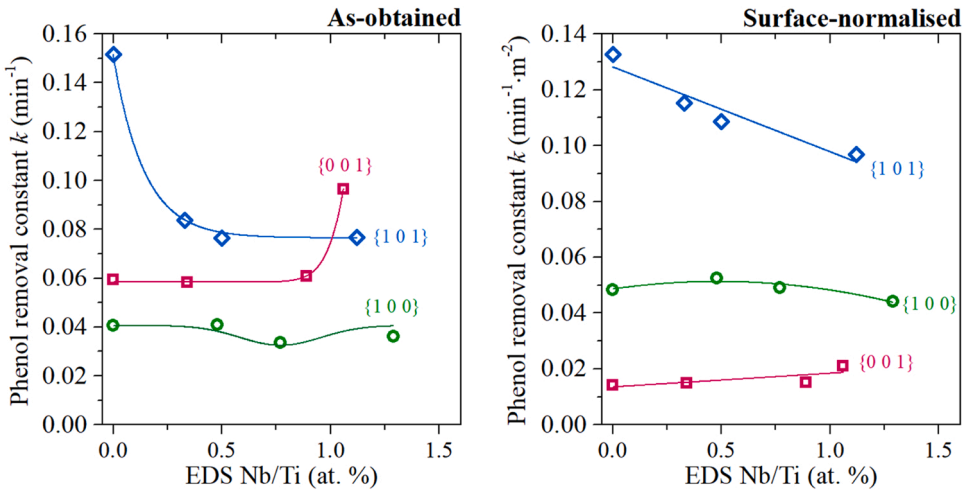

Fig. 10. As-obtained and surface-normalized rate constants of the photocatalytic phenol degradation as the function of exposed crystal facet and Nb concentration. Lines are added as guides. Detailed data is shown in Fig. S10 in the SI.

structures is {1 0 1} > {1 0 0} > {0 0 1}, which especially correlated with the high surface trapping of both electrons and holes on the {1 0 1} facets resulting in their high activity [19,91,92]. However, similarly to the 4-nitrophneol reduction, Nb presence decreased the observed rate constant for these samples, again independently on the surface development. For the remaining two series, niobium introduction affected their activity very slightly and no clear negative effect was observed. On the other hand, some positive effect might be seen, depending if surface normalization was considered. Specifically, {0 0 1} sample modified with the largest amount of Nb showed visible activity enhancement when its surface area was not considered. However, we have previously noted that high phenol degradation rates over these particular facets show general dependence on the high surface area, when synthesis was performed in the same environment [93]. Therefore, some effect of the surface area development might be expected in this case. Independently of the surface area, the Nb effect on phenol degradation is the lowest for the {1 0 0} facets.

Ultimately, it was found that the Nb effect is quite similar for both photoreduction and photodegradation processes. However, the reduction is more sensitive to its presence. The overall results suggest that excess electrons introduced to the TiO_2 photocatalyst can enhance its activity, but only when it does not compromise the reactivity of the co-generated holes. In this case, it is expected only for the {0 0 1} and {1 0 0} facets, which show oxidative character and prefer to trap h^+ in their non-modified form. Finally, calculated apparent quantum efficiencies for the presented results are summarized in the Table 5.

4. Conclusions

Three anatase nanostructures, exposing the majority of the {0 0 1}, {1 0 0}, and {1 0 1} facets were successfully prepared by different conditions of the hydrothermal method. Moreover, the faceted TiO_2 samples were doped with Nb, which allowed us to study the self-trapping of the excess electrons in the photocatalyst structure in the ground state. Based on the performed structural, morphological, and elemental analysis, the formation of a single-phase anatase was confirmed with no secondary Nb-phase. The surface trapping at the Ti sites was observed only for the {1 0 1} facets under the non-vacuum conditions, which resulted in the visible absorption increase in the vis-NIR region (blue coloration), distortion of the EPR signal for the g < 1.99, as well as the disappearance of the "empty" surface electron traps during the RDB-PAS analysis. Simultaneously, no oxygen deficiency was noticed in these samples. For the {0 0 1} facets, introduced electrons localize strictly on the bulk Ti, while for the {1 0 0} ones, they either delocalized over the conduction band states or became trapped at the bulk Ti. The highest activity was observed for the anatase exposing {1 0 1} facets. However, for such octahedral anatase particles exposing {1 0 1} facets, Nb presence decreased activity in both phenol oxidation and 4-nitrophenol reduction reactions. On the other hand, for the {0 0 1} and {1 0 0} series, the introduction of Nb promoted their reactivity, with a maximum depending on the Nb amount. For all samples, the Nb effect is more clear in the reaction of 4-nitrophenol reduction than in phenol photodegradation.

Described results present two important conclusions for further studies. First of all, it experimentally confirms that possible localisation of excess electrons in the photocatalyst structure depend both on the surface structure and the presence of interface species. Especially, results obtained under the vacuum and non-vacuum conditions are different, showing competition between e^- trapping on Nb or Ti sites. With respect to the photocatalyst preparation, it proves that the observed doping effect on the activity might be connected with the photocatalyst surface structure and the charge carriers introduced with the dopant. Empirically, it shows that the positive effect of the electron-donating dopant on the photoreduction process can be obtained for the oxidative TiO_2 facets. Therefore, these findings might be introduced to other photocatalysts/dopants systems to tailor their properties and increase application potential.

Table 5
Calculated apparent quantum efficiencies (%) for the analyzed samples.

Sample	4-nitrophenol reduction 30 min			Phenol degradation 5 min		
	{0 0 1}	{1 0 0}	{1 0 1}	{0 0 1}	{1 0 0}	{1 0 1}
Bare	2.90	0.13	5.94	1.09	0.72	1.85
0.5 % Nb	4.75	0.79	3.27	0.97	0.84	1.10
1.0 % Nb	4.13	0.49	2.69	1.15	0.55	1.39
1.5 % Nb	2.88	0.51	1.22	1.83	0.63	1.28

CRediT authorship contribution statement

Szymon Dudziak: Conceptualization, Methodology, Investigation, Formal analysis, Draft preparation, Writing – Review & Editing, Visualization, Funding acquisition. **Ewa Kowalska:** Formal analysis, Draft preparation, Writing – Review & Editing. **Kunlei Wang:** Investigation, Formal Analysis, Visualization. **Jakub Karczewski:** Investigation, Writing – Review & Editing. **Mirosław Sawczak:** Investigation. **Bunsho Ohtani:** Methodology, Investigation, Formal analysis, Writing – Review & Editing, Visualization. **Anna Zielińska-Jurek:** Methodology, Writing Review & Editing, Supervision, Project administration, Funding

acquisition.

Declaration of Competing Interest

The authors declare the following financial interests/personal relationships which may be considered as potential competing interests. Szymon Dudziak reports financial support was provided by National Science Centre Poland. Anna Zielinska-Jurek reports financial support was provided by National Science Centre Poland.

Data availability

Data will be made available on request.

Acknowledgements

The research was financially supported by the Polish National Science Centre grant no. NCN 2021/41/N/ST5/03447. AZJ is grateful for the financial support from the Polish National Science Centre grant no. NCN 2021/43/B/ST5/02983. Financial support from Gdansk University of Technology under the Oxygenium program supporting open-access publications is acknowledged.

Appendix A. Supporting information

Supplementary data associated with this article can be found in the online version at doi:10.1016/j.apcatb.2023.122448.

References

[1] J. Pan, G. Liu, G.Q. Lu, H.M. Cheng, On the true photoreactivity order of {001}, {010}, and {101} facets of anatase TiO_2 crystals, Angew. Chem. - Int. Ed. 50 (2011) 2133–2137.
[2] M. Lazzeri, A. Vittadini, A. Selloni, Structure and energetics of stoichiometric TiO_2 anatase surfaces, Phys. Rev. B - Condens. Matter Mater. Phys. 63 (2001) 1554091–1554099.
[3] Y. Cao, Q. Li, C. Li, J. Li, J. Yang, Surface heterojunction between (001) and (101) facets of ultrafine anatase TiO_2 nanocrystals for highly efficient photoreduction CO_2 to CH4, Appl. Catal. B Environ. 198 (2016) 378–388.
[4] P. Mikrut, M. Kobielusz, W. Macyk, Spectroelectrochemical characterization of euhedral anatase TiO_2 crystals – implications for photoelectrochemical and photocatalytic properties of {001} {100} and {101} facets, Electrochim. Acta 310 (2019) 256–265.
[5] D. Zhang, S. Wang, J. Zhu, H. Li, Y. Lu, WO_3 nanocrystals with tunable percentage of (001)-facet exposure, Appl. Catal. B Environ. 123–124 (2012) 398–404.
[6] M. Huang, Y. Yan, W. Feng, S. Weng, Z. Zheng, X. Fu, P. Liu, Controllable tuning various ratios of ZnO polar facets by crystal seed-assisted growth and their photocatalytic activity, Cryst. Growth Des. 14 (2014) 2179–2186.
[7] H.B. Jiang, Q. Cuan, C.Z. Wen, J. Xing, D. Wu, X.Q. Gong, C. Li, H.G. Yang, Anatase TiO_2 crystals with exposed high-index facets, Angew. Chem. - Int. Ed. 50 (2011) 3764–3768.
[8] M. Kowalkińska, S. Dudziak, J. Karczewski, J. Ryl, G. Trykowski, A. Zielińska-Jurek, Facet effect of TiO_2 nanostructures from $TiOF_2$ and their photocatalytic activity, Chem. Eng. J. 404 (2021), 126493.
[9] A. Grzegórska, P. Głuchowski, J. Karczewski, J. Ryl, I. Wysocka, K. Siuzdak, G. Trykowski, K. Grochowska, A. Zielińska-Jurek, Enhanced photocatalytic activity of accordion-like layered Ti_3C_2 (MXene) coupled with Fe-modified decahedral anatase particles exposing {1 0 1} and {0 0 1} facets, Chem. Eng. J. 426 (2021), 130801.
[10] T. Takata, J. Jiang, Y. Sakata, M. Nakabayashi, N. Shibata, V. Nandal, K. Seki, T. Hisatomi, K. Domen, Photocatalytic water splitting with a quantum efficiency of almost unity, Nature 581 (2020) 411–414.
[11] X.H. Yang, Z. Li, C. Sun, H.G. Yang, C. Li, Hydrothermal stability of {001} faceted anatase TiO2, Chem. Mater. 23 (2011) 3486–3494.
[12] A. Ballestas-Barrientos, X. Li, S. Yick, A.F. Masters, T. Maschmeyer, Optimised heterojunctions between [100]-oriented rutile TiO_2 arrays and {001} faceted anatase nanodomains for enhanced photoelectrochemical activity, Sustain. Energy Fuels 2 (2018) 1463–1473.
[13] Q.D. Truong, H.T. Hoa, T.S. Le, Rutile TiO_2 nanocrystals with exposed {3 3 1} facets for enhanced photocatalytic CO_2 reduction activity, J. Colloid Interface Sci. 504 (2017) 223–229.
[14] J. Mao, L. Ye, K. Li, X. Zhang, J. Liu, T. Peng, L. Zan, Pt-loading reverses the photocatalytic activity order of anatase TiO_2 {001} and {010} facets for photoreduction of CO_2 to CH_4, Appl. Catal. B Environ. 144 (2014) 855–862.
[15] Q. Chen, H. Wang, C. Wang, R. Guan, R. Duan, Y. Fang, X. Hu, Activation of molecular oxygen in selectively photocatalytic organic conversion upon defective TiO_2 nanosheets with boosted separation of charge carriers, Appl. Catal. B Environ. 262 (2020), 118258.
[16] Y.K. Peng, Y. Hu, H.L. Chou, Y. Fu, I.F. Teixeira, L. Zhang, H. He, S.C.E. Tsang, Mapping surface-modified titania nanoparticles with implications for activity and facet control, Nat. Commun. 8 (2017) 1–13.
[17] Y. Zhou, D.E. Doronkin, M. Chen, S. Wei, J.D. Grunwaldt, Interplay of Pt and crystal facets of TiO_2: CO oxidation activity and operando XAS/DRIFTS studies, ACS Catal. 6 (2016) 7799–7809.
[18] Y. Bi, S. Ouyang, N. Umezawa, J. Cao, J. Ye, Facet effect of single-crystalline Ag_3PO_4 sub-microcrystals on photocatalytic properties, J. Am. Chem. Soc. 133 (2011) 6490–6492.
[19] X. Ma, Y. Dai, M. Guo, B. Huang, Relative photooxidation and photoreduction activities of the {100}, {101}, and {001} surfaces of anatase TiO_2, Langmuir 29 (2013) 13647–13654.
[20] J.J. Carey, K.P. McKenna, Does polaronic self-trapping occur at anatase TiO_2 surfaces? J. Phys. Chem. C. 122 (2018) 27540–27553.
[21] S. Selcuk, A. Selloni, Facet-dependent trapping and dynamics of excess electrons at anatase TiO_2 surfaces and aqueous interfaces, Nat. Mater. 15 (2016) 1107–1112.
[22] S.K. Wallace, K.P. Mckenna, Facet-dependent electron trapping in TiO_2 nanocrystals, J. Phys. Chem. C. 119 (2015) 1913–1920.
[23] G. Fazio, L. Ferrighi, C. Di Valentin, Photoexcited carriers recombination and trapping in spherical vs faceted TiO_2 nanoparticles, Nano Energy 27 (2016) 673–689.
[24] D. Selli, G. Fazio, C. Di Valentin, Using density functional theory to model realistic TiO_2 nanoparticles, their photoactivation and interaction with water, Catalysts 7 (2017) 357.
[25] O. Avilés-García, J. Espino-Valencia, R. Romero, J.L. Rico-Cerda, M. Arroyo-Albiter, R. Natividad, W and Mo doped TiO_2: synthesis, characterization and photocatalytic activity, Fuel 198 (2017) 31–41.
[26] G. Xiang, Z. Yu, Y. Hou, Y. Chen, Z. Peng, L. Sun, L. Sun, Simulated solar-light induced photoelectrocatalytic degradation of bisphenol-A using Fe^{3+}-doped TiO_2 nanotube arrays as a photoanode with simultaneous aeration, Sep. Purif. Technol. 161 (2016) 144–151.
[27] N. Bao, Z. Wei, Z. Ma, F. Liu, G. Yin, Si-doped mesoporous TiO_2 continuous fibers: preparation by centrifugal spinning and photocatalytic properties, J. Hazard. Mater. 174 (2010) 129–136.
[28] T. Simon, M.T. Carlson, J.K. Stolarczyk, J. Feldmann, Electron transfer rate vs recombination losses in photocatalytic H_2 generation on Pt- decorated CdS nanorods, ACS Energy Lett. 1 (2016) 1137–1142.
[29] A. Zielińska-Jurek, M. Klein, J. Hupka, Enhanced visible light photocatalytic activity of Pt/I-TiO_2 in a slurry system and supported on glass packing, Sep. Purif. Technol. 189 (2017) 246–252.
[30] Z. Bielan, S. Dudziak, A. Sulowska, D. Pelczarski, J. Ryl, A. Zielińska-Jurek, Preparation and characterization of defective TiO_2. the effect of the reaction environment on titanium vacancies formation, Materials 13 (2020) 1–25.
[31] P. Mazierski, P.N. Arellano Caicedo, T. Grzyb, A. Mikolajczyk, J.K. Roy, E. Wyrzykowska, Z. Wei, E. Kowalska, T. Puzyn, A. Zaleska-Medynska, J. Nadolna, Experimental and computational study of Tm-doped TiO_2: the effect of Li^+ on vis-response photocatalysis and luminescence, Appl. Catal. B Environ. 252 (2019) 138–151.
[32] H.Y. Wang, J. Chen, F.X. Xiao, J. Zheng, B. Liu, Doping-induced structural evolution from rutile to anatase: formation of Nb-doped anatase TiO_2 nanosheets with high photocatalytic activity, J. Mater. Chem. A 4 (2016) 6926–6932.
[33] X. Han, K. Song, L. Lu, Q. Deng, X. Xia, G. Shao, Limitation and extrapolation correction of the GGA + U formalism: a case study of Nb-doped anatase TiO_2, J. Mater. Chem. C. 1 (2013) 3736–3746.
[34] H.Y. Lee, J. Robertson, Doping and compensation in Nb-Doped anatase and rutile TiO_2, J. Appl. Phys. 113 (2013).
[35] S. Khan, H. Cho, D. Kim, S.S. Han, K.H. Lee, S.H. Cho, T. Song, H. Choi, Defect engineering toward strong photocatalysis of Nb-doped anatase TiO_2: computational predictions and experimental verifications, Appl. Catal. B Environ. 206 (2017) 520–530.
[36] H. Kamisaka, T. Hitosugi, T. Suenaga, T. Hasegawa, K. Yamashita, Density functional theory based first-principle calculation of Nb-doped anatase TiO_2 and its interactions with oxygen vacancies and interstitial oxygen, J. Chem. Phys. (2009) *131*.
[37] A.S. Barnard, L.A. Curtiss, Prediction of TiO_2 nanoparticle phase and shape transitions controlled by surface chemistry, Nano Lett. 5 (2005) 1261–1266.
[38] F. Amano, T. Yasumoto, O.O. Prieto-Mahaney, S. Uchida, T. Shibayama, B. Ohtani, Photocatalytic activity of octahedral single-crystalline mesoparticles of anatase titanium(IV) oxide, Chem. Commun. (No. 17) (2009) 2311–2313.
[39] J. Li, D. Xu, Tetragonal faceted-nanorods of anatase TiO_2 single crystals with a large percentage of active {100} facets, Chem. Commun. 46 (2010) 2301–2303.
[40] C.J. Howard, T.M. Sabine, F. Dickson, Structural and thermal parameters for rutile and anatase, Acta Cryst. B47 (1991) 462–468.
[41] B. Ohtani, Photoacoustic Spectroscopy, in: D.W. Bahnemann, A.O. Patrocinio, C. Colbeau-Justin (Eds.), Springer Handbook of Inorganic Photochemistry, Springer-Nature, 2022, pp. 303–313 (Section B).
[42] M.I. Cabrera, O.M. Alfano, A.E. Cassano, Absorption and scattering coefficients of titanium dioxide participate suspensions in water, J. Phys. Chem. 100 (1996) 20043.
[43] R. Li, X. Zhang, H. Dong, Q. Li, Z. Shuai, W. Hu, Gibbs-Curie-Wulff theorem in organic materials: a case study on the relationship between surface energy and crystal growth, Adv. Mater. 28 (2016) 1697–1702.

[44] M. Zhang, X. Xiao, X. Wang, M. Chen, Y. Lu, M. Liu, L. Chen, Excellent catalysis of TiO_2 nanosheets with high-surface-energy {001} facets on the hydrogen storage properties of MgH_2, Nanoscale 11 (2019) 7465–7473.

[45] X. Han, Q. Kuang, M. Jin, Z. Xie, L. Zheng, Synthesis of titania nanosheets with high percentage of exposed (001) facets and related photocatalytic properties, J. Am. Chem. Soc. 131 (2009) 3152–3153.

[46] M. Maisano, M. Dozzi, M. Coduri, L. Artiglia, Q. Granozzi, E. Selli, Unraveling the multiple effects originating the increased oxidative photoactivity of {001}-facet enriched anatase TiO_2, ACS Appl. Mater. Interfaces 8 (2016) 9745–9754.

[47] Y.J. Yuan, Z.J. Ye, H.W. Lu, B. Hu, Y.H. Li, D.Q. Chen, J.S. Zhong, Z.T. Yu, Z. G. Zou, Constructing anatase TiO_2 nanosheets with exposed (001) facets/layered MoS_2 two-dimensional nanojunctions for enhanced solar hydrogen generation, ACS Catal. 6 (2016) 532–541.

[48] A.S. Barnard, P. Zapol, L.A. Curtiss, Anatase and rutile surfaces with adsorbates representative of acidic and basic conditions, Surf. Sci. 582 (2005) 173–188.

[49] Y. Zhang, C. Li, C. Pan, N + Ni codoped anatase TiO 2 nanocrystals with exposed {001} facets through two-step hydrothermal route, J. Am. Ceram. Soc. 95 (2012) 2951–2956.

[50] T.R. Gordon, M. Cargnello, T. Paik, F. Mangolini, R.T. Weber, P. Fornasiero, C. B. Murray, Nonaqueous synthesis of TiO_2 nanocrystals using TiF_4 to engineer morphology, oxygen vacancy concentration, and photocatalytic activity, J. Am. Chem. Soc. 134 (2012) 6751–6761.

[51] D.S. Bhachu, S. Sathasivam, G. Sankar, D.O. Scanlon, G. Cibin, C.J. Carmalt, I. P. Parkin, G.W. Watson, S.M. Bawaked, A.Y. Obaid, S. Al-Thabaiti, S.N. Basahel, Solution processing route to multifunctional titania thin films: highly conductive and photcatalytically active Nb:TiO_2, Adv. Funct. Mater. 24 (2014) 5075.

[52] X. Lü, W. Yang, Z. Quan, T. Lin, L. Bai, L. Wang, F. Huang, Y. Zhao, Enhanced electron transport in Nb-doped TiO_2 nanoparticles via pressure-induced phase transitions, *J. Am. Chem. Soc.* 136 (2014) 419.

[53] F. Zhao, B. Wang, Y. Tang, H. Ge, Z. Huang, H.K. Liu, Niobium doped anatase TiO_2 as an effective anode material for sodium-ion batteries, J. Mater. Chem. A 3 (2015) 22969.

[54] Y. Wang, H. Zhang, Y. Han, P. Liu, X. Yao, H. Zhao, A selective etching phenomenon on {001} faceted anatase titanium dioxide single crystal surfaces by hydrofluoric acid, Chem. Comm. 47 (2011) 2829.

[55] K. Morawa Eblagon, A. Malaika, K. Ptaszynska, M.F.R. Pereira, J.L. Figueiredo, Impact of thermal treatment of Nb_2O_5 on its performance in glucose dehydration to 5-hydroxymethylfurfural in water, Nanomaterials 10 (2020) 1685.

[56] J. Kuncewicz, B. Ohtani, Titania photocatalysis through two-photon band-gap excitation with built-in rhodium redox mediator, Chem. Commun. 51 (2015) 298–301.

[57] S. Zheng, Z. Wei, K. Yoshiiri, M. Braumüller, B. Ohtani, S. Rau, E. Kowalska, Titania modification with a ruthenium(II) complex and gold nanoparticles for photocatalytic degradation of organic compounds, Photochem. Photobiol. Sci. 15 (2016) 69–79.

[58] L.A. Morais, C. Adán, A.S. Araujo, A.P.M.A. Guedes, J. Marugán, Synthesis, characterization, and photonic efficiency of novel photocatalytic niobium oxide materials, Glob. Chall. 1 (2017) 1700066.

[59] N.P. Ferraz, F.C.D. Marcos, A.E. Nogueira, A.S. Martins, M.R.V. Lanza, E.M. Assaf, Y.J.O. Asencios, Hexagonal-Nb_2O_5/anatase-TiO_2 mixtures and their applications in the removal of methylene blue dye under various conditions, Mater. Chem. Phys. 198 (2017) 331–340.

[60] A.M. Raba, J. Bautista-Ruíz, M.R. Joya, Synthesis and structural properties of niobium pentoxide powders: a comparative study of the growth process, Mater. Res. 19 (2016) 1381–1387.

[61] J. Yan, G. Wu, N. Guan, L. Li, Nb_2O_5/TiO_2 heterojunctions: synthesis strategy and photocatalytic activity, Appl. Catal. B Environ. 152–153 (2014) 280–288.

[62] X. Bi, G. Du, A. Kalam, D. Sun, W. Zhao, Y. Yu, Q. Su, B. Xu, A.G. Al-Sehemi, Constructing anatase TiO_2/amorphous Nb_2O_5 heterostructures to enhance photocatalytic degradation of acetaminophen and nitrogen oxide, J. Colloid Interface Sci. 601 (2021) 346–354.

[63] S. Zhang, S. Cao, T. Zhang, J.Y. Lee, Plasmonic oxygen-deficient TiO_{2-x} nanocrystals for dual-band electrochromic smart windows with efficient energy recycling, Adv. Mater. (2020) *32*.

[64] G. Liu, H.G. Yang, X. Wang, L. Cheng, H. Lu, L. Wang, G.Q. Lu, H.M. Cheng, Enhanced photoactivity of oxygen-deficient anatase TiO_2 sheets with dominant {001} facets, J. Phys. Chem. C. 113 (2009) 21784–21788.

[65] L. Liu, Y. Jiang, H. Zhao, J. Chen, J. Cheng, K. Yang, Y. Li, Engineering coexposed {001} and {101} facets in oxygen-deficient TiO_2 nanocrystals for enhanced CO_2 photoreduction under visible light, ACS Catal. 6 (2016) 1097–1108.

[66] G. Zhu, Y. Shan, T. Lin, W. Zhao, J. Xu, Z. Tian, H. Zhang, C. Zheng, F. Huang, Hydrogenated blue titania with high solar absorption and greatly improved photocatalysis, Nanoscale 8 (2016) 4705–4712.

[67] S.T. Myung, M. Kikuchi, C.S. Yoon, H. Yashiro, S.J. Kim, Y.K. Sun, B. Scrosati, Black anatase titania enabling ultra high cycling rates for rechargeable lithium batteries, Energy Environ. Sci. 6 (2013) 2609.

[68] H. Nogawa, T. Hitosugi, A. Chikamatsu, S. Nakao, Y. Hirose, T. Shimada, H. Kumigashira, M. Oshima, T. Hasegawa, Carrier compensation by excess oxygen atoms in anatase $Ti_{0.94}Nb_{0.06}O_{2+\delta}$ epitaxial thin films, Jpn. J. Appl. Phys. 49 (2010), 041102.

[69] L. Kong, C. Wang, H. Zheng, X. Zhang, Y. Liu, Defect-induced yellow color in Nb-doped TiO_2 and its impact on visible-light photocatalysis, J. Phys. Chem. C. 119 (2015) 16623–16632.

[70] V. Etacheri, M.K. Seery, S.J. Hinder, S.C. Pillai, Oxygen rich titania: a dopant free, high temperature stable, and visible-light active anatase photocatalyst, Adv. Funct. Mater. 21 (2011) 3744–3752.

[71] Q. Wu, F. Huang, M. Zhao, J. Xu, J. Zhou, Y. Wang, Ultra-small yellow defective TiO_2 nanoparticles for co-catalyst free photocatalytic hydrogen production, Nano Energy 24 (2016) 63–71.

[72] F. Pellegrino, E. Morra, L. Mino, G. Martra, M. Chiesa, V. Maurino, Surface and bulk distribution of fluorides and Ti^{3+} species in TiO_2 nanosheets: implications on charge carrier dynamics and photocatalysis, J. Phys. Chem. C. 124 (2020) 3141–3149.

[73] J. Biedrzycki, S. Livraghi, E. Giamello, S. Agnoli, G. Granozzi, Fluorine- and niobium-doped TiO_2: chemical and spectroscopic properties of polycrystalline n-type-doped anatase, J. Phys. Chem. C. 118 (2014) 8462–8473.

[74] M. Chiesa, M.C. Paganini, S. Livraghi, E. Giamello, Charge trapping in TiO_2 polymorphs as seen by electron paramagnetic resonance spectroscopy, Phys. Chem. Chem. Phys. 15 (2013) 9435–9447.

[75] T. Li, Z. Shen, Y. Shu, X. Li, C. Jiang, W. Chen, Facet-dependent evolution of surface defects in anatase TiO_2 by thermal treatment: implications for environmental applications of photocatalysis, Environ. Sci. Nano 6 (2019) 1740–1753.

[76] V. Polliotto, S. Livraghi, E. Giamello, Electron magnetic resonance as a tool to monitor charge separation and reactivity in photocatalytic materials, Res. Chem. Intermed. 44 (2018) 3905–3921.

[77] J.B. Priebe, J. Radnik, A.J.J. Lennox, M.M. Pohl, M. Karnahl, D. Hollmann, K. Grabow, U. Bentrup, H. Junge, M. Beller, A. Brückner, Solar hydrogen production by plasmonic Au-TiO_2 catalysts: impact of synthesis protocol and TiO_2 phase on charge transfer efficiency and H_2 evolution rates, ACS Catal. 5 (2015) 2137–2148.

[78] C.P. Kumar, N.O. Gopal, T.C. Wang, EPR investigation of TiO_2 nanoparticles with temperature-dependent properties, J. Phys. Chem. B 110 (2006) 5223–5229.

[79] A. Nitta, M. Takashima, N. Murakami, M. Takase, B. Ohtani, Reversed double-beam photoacoustic spectroscopy of metal-oxide powders for estimation of their energy-resolved distribution of electron traps and electronic-band structure, Electrochim. Acta 264 (2018) 83–90.

[80] A. Nitta, M. Takashima, M. Takase, B. Ohtani, Identification and characterization of titania photocatalyst powders using their energy-resolved distribution of electron traps as a fingerprint, Catal. Today 321–322 (2019) 2–8.

[81] Y. Shen, A. Nitta, M. Takashima, B. Ohtani, Do particles interact electronically? Proof of interparticle charge-transfer excitation between adjoined anatase and rutile particles, Chem. Lett. 50 (2021) 80–83.

[82] N. Serpone, A. Salinaro, Terminology, relative photonic efficiencies and quantum yields in heterogeneous photocatalysis. Part I: suggested protocol (technical report), Pure Appl. Chem. 71 (1999) 303.

[83] J. Colina-Márquez, F. Machua-Martínez, G. Li Puma, Radiation absorption and optimization of solar photocatalytic reactors for environmental applications, Environ. Sci. Technol. 44 (2010) 5112–5120.

[84] A. Brucato, A.E. Cassano, F. Grisafi, G. Montante, L. RIzzuti, G. Vella, Estimating radiant fields in flat heterogeneous photoreactors by the six-flux model, AIChE J. 52 (2006) 3882–3890.

[85] S. Yurdakal, V. Loddo, B.B. Ferrer, G. Palmisano, V. Augugliaro, J.G. Farreras, L. Palmisano, Optical properties of TiO_2 suspensions: influence of pH and powder concentration on mean particle size, Ind. Eng. Chem. Res. 46 (2007) 7620.

[86] M.L. Satuf, R.J. Brandi, A.E. Cassano, O.M. Alfano, Experimental method to evaluate the optical properties of aqueous titanium dioxide suspensions, Ind. Eng. Chem. Res. 44 (2005) 6643.

[87] R. Acosta-Herazo, M.A. Mueses, G. Li Puma, F. Machuca-Martínez, Impact of photocatalyst optical properties on the efficiency of solar photocatalytic reactors rationalized by the concepts of initial rate of photon absorption (IRPA) dimensionless boundary layer of photon absorption and apparent optical thickness, Chem. Eng. J. 356 (2019) 839–849.

[88] G. Li Puma, A. Brucato, Dimensionless analysis of slurry photocatalytic reactors using two-flux and six-flux radiation absorption-scattering models, Cat. Today 122 (2007) 78–80.

[89] L. Delforce, E. Hofmann, V. Nardello-Rataj, J.M. Aubry, TiO_2 nanoparticle dispersions in water and nonaqueous solvents studied by gravitational sedimentation nnalysis: complementarity of hansen parameters and DLVO interpretations, Colloids Surf. A: Physicochem. Eng. Asp. 628 (2021), 127333.

[90] Y. Nosaka, A.Y. Nosaka, Generation and detection of reactive oxygen species in photocatalysis, Chem. Rev. 117 (2017) 11302–11336.

[91] S. Dudziak, M. Kowalkińska, J. Karczewski, M. Pisarek, J.D. Gouveia, J.R. B. Gomes, A. Zielińska-Jurek, Surface and trapping energies as predictors for the photocatalytic degradation of aromatic organic pollutants, J. Phys. Chem. C. 126 (2022) 14859–14877.

[92] M. Kowalkińska, K. Sikora, M. Łapiński, J. Karczewski, A. Zielińska-Jurek, Non-toxic fluorine-doped TiO_2 nanocrystals from $TiOF_2$ for facet-dependent naproxen degradation, Catal. Today, DOI: ⟨https://doi.org/10.1016/j.cattod.2022.11.020⟩,

[93] S. Dudziak, M. Kowalkińska, J. Karczewski, M. Pisarek, K. Siuzdak, A. Kubiak, K. Siwińska-Ciesielczyk, A. Zielińska-Jurek, Solvothermal growth of {0 0 1} exposed anatase nanosheets and their ability to mineralize organic pollutants. the effect of alcohol type and content on the nucleation and growth of TiO_2 nanostructures, Appl. Surf. Sci. 563 (2021), 150360.